



# Assessment of Incident Power Density on Spherical Head Model up to 100 GHz

Ante Lojić Kapetanović , *Graduate Student Member, IEEE*, and Dragan Poljak , *Senior Member, IEEE*

**Abstract**—This article presents a technique for the accurate assessment of the spatially averaged incident power density (IPD) on a spherical human head model from 3.5 to 100 GHz. The spatially-averaged IPD is defined either by averaging components of the power density vector normal to an evaluation surface, or by averaging its norm. The electromagnetic exposure assessment is provided for a dipole antenna placed at a separation distance of 2–150 mm from the model. We compare the IPD averaged over a proposed spherical surface with differently positioned planar surfaces. Results show that, for appropriate settings of the exposure above 6 GHz, the IPD averaged on a spherical surface is up to 12% larger for the normal definition, while marginally lower for the norm definition. In the worst case scenario, the spatially averaged IPD on a spherical surface is up to about 30% larger regardless of the definition. Comparative analysis between the definitions of the IPD averaged on a spherical model demonstrates that the norm definition yields significantly larger values in the reactive near field at characteristic frequencies, whereby this difference is marginal out of the reactive near field.

**Index Terms**—Compliance assessment, human head, incident power density (IPD), millimeter waves, radiation safety.

## I. INTRODUCTION

THE fifth generation (5G) wireless communication systems have been actively deployed worldwide [1] by operating in either sub-6 GHz frequency bands (e.g., sub-1 GHz range that supports widespread coverage, 3.3–4.2 GHz range supported by majority of commercial 5G networks, etc.) or in millimeter wave (mmW) spectrum due to the large available bandwidth and high data rates [2]. At the same time, the widespread use of personal and on-body devices operating at mmW causes a growing public concern with regards to potential negative health effects [3]. The mmW spectrum corresponds to the frequency range between 30 and 300 GHz, and is defined as the extremely high frequency (EHF) band by the International Telecommunication Union. The electromagnetic (EM) radiation in the EHF band does not carry sufficient energy per photon to cause the ionization during the interaction with biological tissue, and, as such, is considered

nonionizing [4]. The only hazardous effect that EM waves in the EHF band may cause under certain conditions is the excessive heating of tissue [5].

Theoretically, EM waves with such a small wavelength are able to penetrate at most 1 mm into the human skin and the fact that more than 90% of the total energy is dissipated in the outermost layer of skin drove international guidelines [6] and IEEE standards [7] for human protection from EM fields to be revisited recently. The dose metric for quantification of internal EM exposure is defined as the basic restriction (BR) [6] or the dosimetric reference level (DRL) [7]. The reference level (RL) [6] or the exposure reference level (ERL) [7] is derived upon the BR/DRL to quantify external exposure and mitigate the issue of internal measuring. The most notable update of both guidelines and standards is the introduction of the new BR/DRL physical quantity above the transition frequency of 6 GHz. The absorbed power density (APD) [6] or epithelial power density [7] (hereafter the abbreviation APD is used for the epithelial power density as well to facilitate readability) represents the power per unit area deposited over irradiated surface of the tissue and should be averaged over a square  $4 \text{ cm}^2$  area to account for the consistency with the volume averaged specific absorption rate (SAR) at lower frequencies [8]. Above 30 GHz, the averaging should be additionally performed over a square  $1 \text{ cm}^2$  area and the APD should not exceed twice the value for a square  $4 \text{ cm}^2$  area [9]. The associated RL/ERL is defined in terms of the spatially averaged IPD, which represents the external exposure quantity defined as the free space approximation of the APD to conduct compliance assessments safer and more practical [10].

The sole purpose of the IPD is to correlate the temperature rise on the surface of the skin, and a large body of research literature exist on the topic [11]–[13]. Simple analytical models [14]–[16], as well as more complex numerical models [17], [18], have firmly established the IPD as the valid proxy for the surface temperature elevation. However, there still exists ambiguities such as: 1) which component of the IPD—the norm or the normal component, correlates more with the thermal elevation in human body tissues and represents a more realistic estimate; and 2) how properties of realistic tissues, e.g., irregularities of surface geometry, curvature, edges, etc., affect the averaging of the power density. Many recent studies explored the two possible definitions of the spatially averaged IPD [17]–[24]. The guide from Working Group 5 within the IEEE/ICES TC95/SC6 [25] shed some light on issue 1, where it is numerically determined that both definitions are comparable if the assessment has been conducted for small incidence angles. Issue 2 is yet to be

Manuscript received 2 March 2022; revised 20 April 2022 and 7 June 2022; accepted 11 June 2022. Date of publication 4 July 2022; date of current version 13 October 2022. This work was supported by the European Regional Development Fund under the grant KK.01.1.1.01.0009 (DATACROSS). (Corresponding author: Ante Lojić Kapetanović.)

The authors are with the Faculty of Electrical Engineering, Mechanical Engineering and Naval Architecture (FESB), University of Split, 21000 Split, Croatia (e-mail: alojic00@fesb.hr; dpoljak@fesb.hr).

Color versions of one or more figures in this article are available at <https://doi.org/10.1109/TEM.2022.3183071>.

Digital Object Identifier 10.1109/TEM.2022.3183071

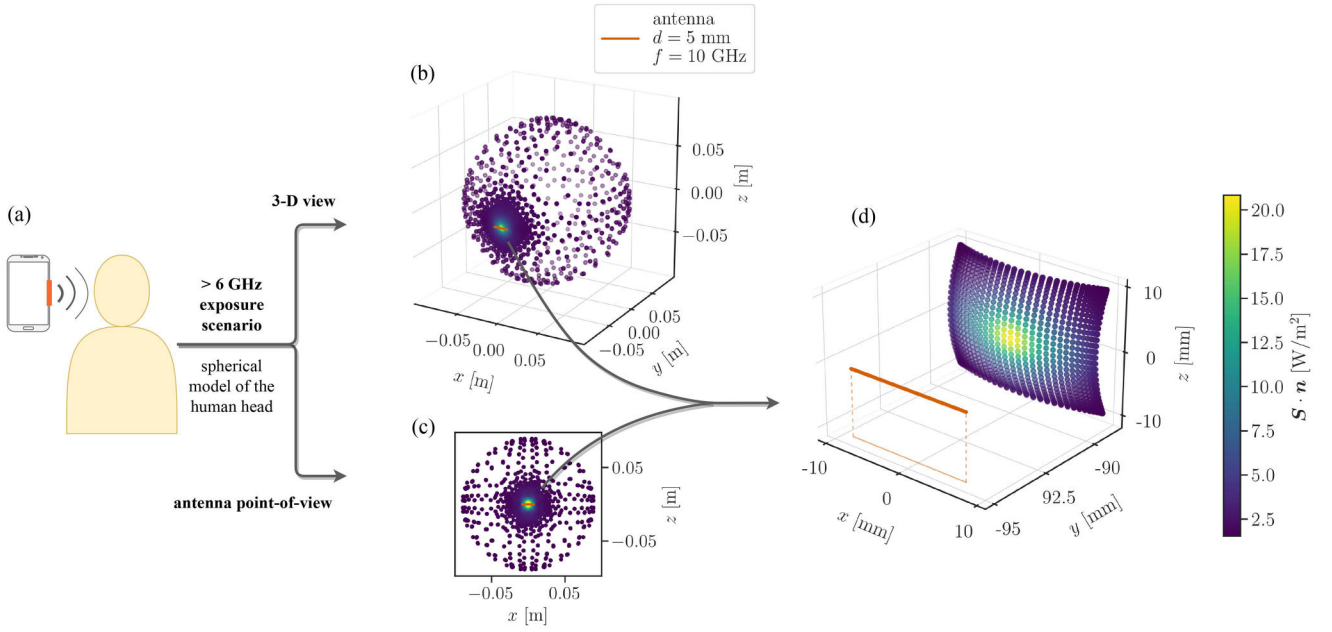


Fig. 1. Overview of the exposure scenario: (a) a 5G hand-held device is placed in the immediate vicinity of a human head; (b) spatial distribution of the magnitude of the time-averaged Poynting vector on the surface of a spherical model of a human head where the radiation source is modelled as a half-wavelength dipole antenna operating at 10 GHz and placed at a separation distance of 5 mm; (c) spatial distribution of the magnitude of the time-averaged Poynting vector on the directly exposed surface; (d) spatial distribution of the normal component of the time-averaged Poynting vector on the 4 cm<sup>2</sup> averaging surface.

explored since all studies, to the best of our knowledge, use planar single- or multilayer phantoms.

Experimental studies have been performed in humans and animals, where the main purpose is to determine thresholds of adverse health effects by using the spatially averaged IPD. In [26], the threshold for the heat inducing pain sensation of 12.5 kW/m<sup>2</sup> at 94 GHz after 3 s exposure has been found. The surface temperature raised up 9.9 °C from the baseline and has been shown to be positively correlated with the IPD. More recent animal study [27] has reported that adverse radiation effects in terms of ocular damage on pigmented rabbit eyes occur for the IPD greater than 1.4 kW/m<sup>2</sup> at 40 GHz, 75 GHz, and 95 GHz. Results have also shown that below 500 W/m<sup>2</sup> no damage occurred. Both studies used planar surfaces to evaluate the spatially averaged IPD on. Even though results are consistent with guidelines and standards, it is of the utmost importance to account for the inherent nonplanar shape of exposed body parts with more realistic tissue-equivalent models and averaging surfaces for retrieval of dosimetric quantities. In [28], averaging across canonical curved surfaces and a forearm model is performed. However, as the finite difference approach has been utilized in the aforementioned study, tissue is represented with voxel models, which are known to suffer from numerical errors due to stair-casing approximations of the curvature [29].

The work presented in this article proposes an accurate method to average the IPD on a surface of a spherical model of a human head, which inherently represents a more sophisticated approximation and is closer to the actual geometry of an averaging surface. Both definitions of the spatially averaged IPD are taken into consideration to validate our approach. In the following section, the model of an antenna and the spherical

head model are presented, along with the numerical approach for the assessment of the IPD on a spherical surface. In Section III, computational results of the IPD are given and compared for the range of frequencies between 3.5 GHz and 100 GHz at different separation distances between averaging surfaces and the antenna. Intercomparison of the IPD for differently positioned planar averaging surfaces and a spherical surface is provided and discussed in detail. Finally, Section IV concludes this article.

## II. MATERIALS AND METHODS

### A. Electromagnetic Model

A center-fed half-wavelength dipole antenna is driven by a voltage source set to 1 V, and is used as the radiation source for the EM exposure simulation. The current distribution is governed by the Pocklington integro-differential equation, solution of which is carried out by means of the Galerkin-Bubnov indirect boundary element method [30]. Mathematical details are available in Appendix A.

We consider an exposure scenario, where the radiation source is a 5G hand-held device placed in the immediate vicinity of a human head, shown schematically in Fig. 1(a). A human head is represented by the spherical model with a radius set to 9 cm to match the vertical distance from the nasal root depression between the eyes to the level of the top of the head for an average adult male [31]. The model is sampled as a point cloud resulting in 2312 surface points in total, where the spatial density of points depends on the relative position to the antenna. Mathematical details of EM field assessment over the surface of the model are provided in Appendix A.

### B. Assessment and Averaging of Incident Power Density

The time-averaged Poynting vector represents the direction and the density of EM power flow and is defined as

$$\mathbf{S} = \frac{1}{2} \Re [\mathbf{E} \times \mathbf{H}^*] \quad (1)$$

where  $\mathbf{E}$  and  $\mathbf{H}$  are peak values of the complex phasor electric and magnetic field, respectively, and  $*$  is the complex conjugate operator. The magnitude of  $\mathbf{S}$  across the surface of the head model for the case in which a half-wavelength dipole antenna operates at 10 GHz is shown in three-dimension (3-D) view in Fig. 1(b), and from the antenna point-of-view in Fig. 1(c).

According to [25], the IPD is computed as the spatial-average of the normal component of  $\mathbf{S}$  over the averaging surface area,  $A$

$$sPD_n = \frac{1}{A} \iint_A \mathbf{S} \cdot \mathbf{n} \, dA \quad (2)$$

where  $\mathbf{n}$  is the unit vector normal to the averaging surface and  $dA$  is the differential area element. The spatial distribution of  $\mathbf{S} \cdot \mathbf{n}$  across  $A$  is shown in Fig. 1(d).

Another definition of the IPD as the spatial-average of the norm of  $\mathbf{S}$ , discussed in detail in [25] and explored computationally in [24], is given as follows:

$$sPD_{tot} = \frac{1}{A} \iint_A |\mathbf{S}| \, dA. \quad (3)$$

Even though this definition does not have a clear physical interpretation, it is proven to be more conservative with respect to (2) in free space on the planar evaluation surface [25]. As such, it could provide better estimate once the presence of the tissue is considered, especially in the near field region of a radiating source, where the tangential components of  $\mathbf{S}$  are not negligible compared to normal components.

For a spherical averaging surface, the entire geometry should be transformed from Cartesian  $(x, y, z)$  to spherical  $(r, \theta, \varphi)$  coordinate system. According to ISO 80000-2:2019 convention,  $r$  represents the radial distance, i.e., the distance to origin,  $\theta$  is the polar angle, and  $\varphi$  is the angle of rotation from the initial meridian plane, i.e., azimuthal angle. Assuming the radius is constant, the parametric representation of the surface is then written as

$$\mathbf{v}(\theta, \varphi) = r \sin(\theta) \cos(\varphi) \hat{e}_x + r \sin(\theta) \sin(\varphi) \hat{e}_y + r \cos(\theta) \hat{e}_z \quad (4)$$

Unit vector normal to the parametric surface is given as follows:

$$\mathbf{n} = -\frac{\mathbf{v}_\theta \times \mathbf{v}_\varphi}{|\mathbf{v}_\theta \times \mathbf{v}_\varphi|} \quad (5)$$

where  $\mathbf{v}_\theta \times \mathbf{v}_\varphi$  is the cross product between partial derivatives of the parametric surface and it results in the vector normal to the tangent plane at a particular point. The spatial distribution of the unit vector normal to the averaging surface is shown in Fig. 2.

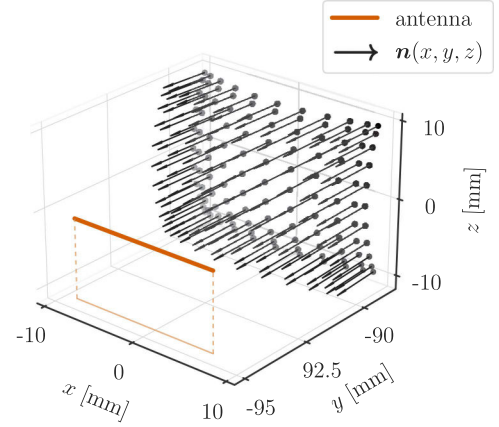


Fig. 2. Spatial distribution of the unit vector normal to the spherical  $4 \text{ cm}^2$  averaging surface at a distance of 5 mm from the half-wavelength dipole antenna operating at 10 GHz.

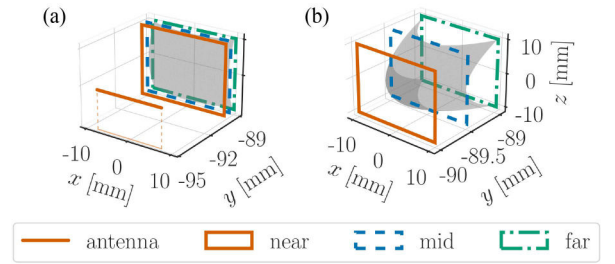


Fig. 3. Positional relationship between a spherical and planar surfaces: (a) planar averaging surfaces are placed at the same distance as the nearest point ("near," full line), middle points ("mid," dash line), and farthest points ("far," dot-dash line) of a spherical surface relative to the antenna, respectively; (b) zoomed display of averaging surfaces.

Equation (2) is then redefined as a dot product between  $\mathbf{S}$  and the unit vector field normal to the parametric surface,  $\mathbf{v}$

$$sPD_n = \frac{1}{A} \iint \mathbf{S}(\mathbf{v}) \cdot (\mathbf{v}_\theta \times \mathbf{v}_\varphi) \, d\theta d\varphi \quad (6)$$

while (3) is simply rewritten as

$$sPD_{tot} = \frac{1}{A} \iint |\mathbf{S}(\mathbf{v})| r^2 \sin(\theta) \, d\theta d\varphi \quad (7)$$

where the factor  $r^2 \sin(\theta)$  is derived upon the definition of the integral element spanning from  $\theta$  to  $\theta + d\theta$  and  $\varphi$  to  $\varphi + d\varphi$  on a spherical surface at constant  $r$ .

To compute the solution of (6) and (7) numerically, the two-dimension (2-D) Gauss-Legendre quadrature is utilized to define a suitable choice of integration nodes across the parametric surface. The surface integral is then approximated as a sum of incremental contributions across the parametric surface at integration nodes selected as roots of the 11<sup>th</sup> degree Legendre polynomials, scaled with proper weights derived at each corresponding node [32].

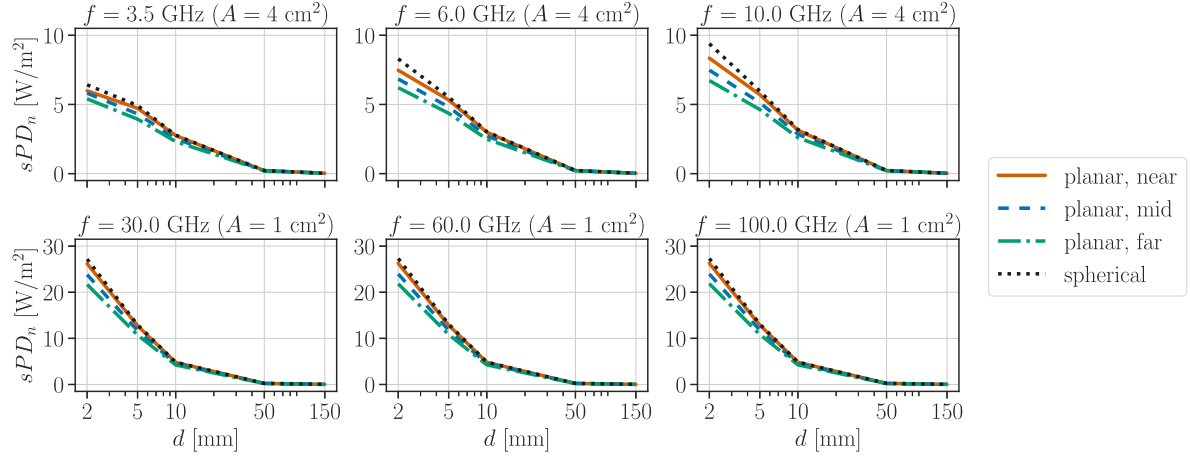


Fig. 4.  $sPD_n$  averaged over three planar surfaces (“near,” “mid” and “far”) and a spherical surface as a function of the separation distance from the antenna at 3.5 GHz, 6 GHz, and 10 GHz (first row), and at 30 GHz, 60 GHz, and 100 GHz (second row).

### III. RESULTS AND DISCUSSION

We analyze the IPD averaged over a spherical surface in comparison to planar surfaces placed in three different locations relative to a spherical one, see Fig. 3. The “near” planar averaging surface is placed at the distance of the nearest point on the spherical averaging surface relative to the antenna position. This means that the “near” planar surface lies on a tangent plane to the spherical averaging surface at this particular point. The “mid” planar averaging surface is located on a plane intersecting the spherical averaging surface at four points in the middle—between the nearest point and four farthest points on the surface of the spherical averaging surface relative to the antenna position. Finally, the “far” planar averaging surface intersects the spherical averaging surface at four farthest points relative to the antenna position. From 3.5 to 30 GHz, the IPD is averaged over a surface area of  $4 \text{ cm}^2$ , and at 30 GHz or above, an area is reduced to  $1 \text{ cm}^2$ . Although neither guidelines nor standards consider the spatially averaged IPD as the RL/ERL at 3.5 GHz, this frequency is also included in the analysis as it is characteristic of majority of 5G commercial solutions that rely on sub-6 GHz frequency bands, some of which are traditionally used by preceding generations of wireless communication systems. Separation distances between the antenna and averaging surfaces,  $d$ , range from 2 to 150 mm.

#### A. Normal Component Definition

Results comparing  $sPD_n$  averaged over a spherical surface and three planar surfaces as a function of the separation distance from the antenna,  $d$ , are shown in Fig. 4. With an increase in the separation distance,  $sPD_n$  decreases monotonically at each frequency considered in the analysis, regardless of the shape of an averaging surface. The IPD averaged over a spherical surface is larger in comparison to either planar surface. This is especially pronounced at 10 GHz, where the relative difference may reach up to 28.35%, 20.35% and 11.11% for the “far,” “mid,” and “near” planar surfaces at  $d = 2 \text{ mm}$ , respectively. At 3.5 GHz, the relative difference for the worst case scenario (the “far” planar surface at  $d = 5 \text{ mm}$ ) is 20.09%. Note that this particular

frequency is the only one considered in the analysis, where the relative difference is not the largest at  $d = 2 \text{ mm}$  for the “far” and “mid” planar surfaces. For more appropriate settings, where the “near” planar surface is considered, the relative difference is at most 6.68% at  $d = 2 \text{ mm}$ . After reducing the averaging area to  $1 \text{ cm}^2$  at 30 GHz the difference becomes less significant ranging from  $\sim 4\%$  for the “near” planar surface to  $\sim 13\%$  for the “far” planar surface at  $d = 2 \text{ mm}$ . Regardless of the frequency, negligible differences between  $sPD_n$  on the spherical and “near” planar averaging surfaces (within 1%) are present at  $d \geq 50 \text{ mm}$ . For a full overview of the relative difference between the IPD averaged over a spherical and three planar surfaces, see Fig. 5.

#### B. Norm Definition

Results comparing  $sPD_{tot}$  averaged on a spherical surface and three planar surfaces as a function of the separation distance from the antenna,  $d$ , are shown in Fig. 6. Similar to  $sPD_n$ ,  $sPD_{tot}$  decreases monotonically with the increased separation distance for all considered averaging surfaces. Another similarity to  $sPD_n$  is the fact that  $sPD_{tot}$  at or above 30 GHz is increased only slightly (within  $0.1 \text{ W/m}^2$  for identical surfaces at corresponding  $d$ ) with an increase in frequency. At such high frequencies, the beam becomes extremely focused in the control averaging surface. Although an increase in individual values of the IPD is present (particularly at the center of the beam), once averaged over the control surface, no significant changes in the spatially averaged IPD occur. Also, this could be further explained, but to a much lesser extent, by the finite resolution of both: the spatial domain, i.e., 2-D evaluation plane on which the averaging is performed, and the choice of the degree of integration. Furthermore, results demonstrate that  $sPD_{tot}$  averaged on a spherical surface is only slightly lower in comparison to  $sPD_{tot}$  averaged on the “near” planar surface at all considered frequencies, while significantly larger in comparison to  $sPD_{tot}$  averaged on the “mid” and “far” planar surfaces. Given the very definition of  $sPD_{tot}$ , where the spatial average of the magnitude of the time-averaged Poynting vector is considered on a control



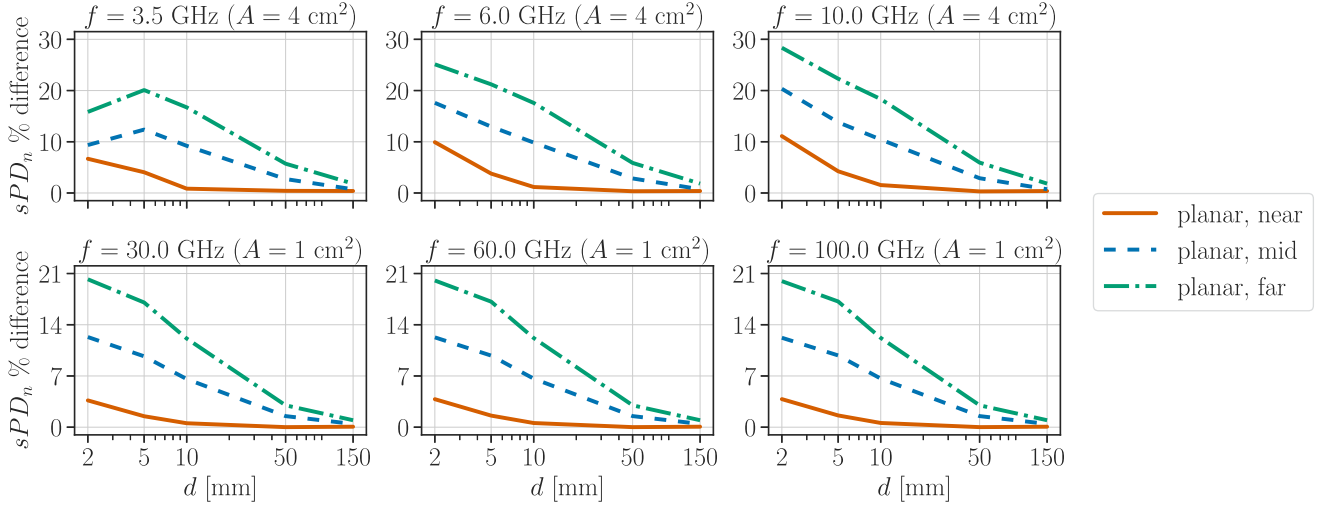


Fig. 5. Relative differences between  $sPD_n$  averaged on a spherical surface and 3 planar surfaces (“near,” “mid,” and “far”) as functions of the separation distance from the antenna at 3.5 GHz, 6 GHz, and 10 GHz (first row), and 30 GHz, 60 GHz, and 100 GHz (second row).

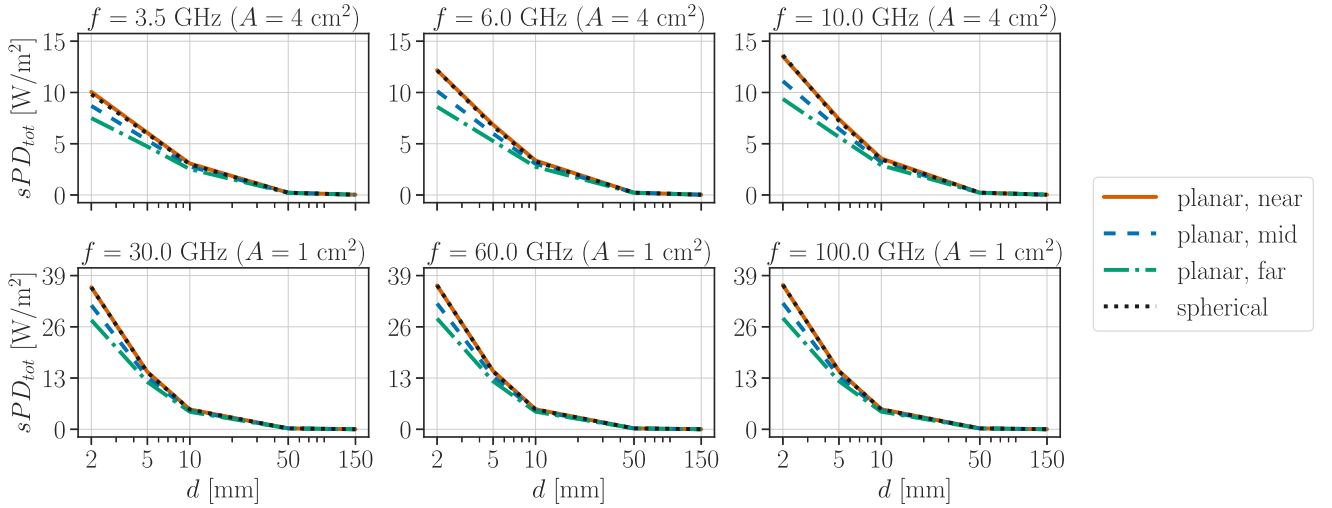


Fig. 6.  $sPD_{tot}$  averaged over three planar surfaces (“near,” “mid,” and “far”) and a spherical surface as a function of the separation distance from the antenna at 3.5 GHz, 6 GHz, and 10 GHz (first row), and at 30 GHz, 60 GHz, and 100 GHz (second row).

surface instead of its normal components, such results are expected. As all three components of the power density vector are treated equally, the spatial distribution of the unit vector normal to the averaging surface does not play a role here unlike in the assessment of  $sPD_n$  and the value of  $sPD_{tot}$  depends only on the separation distance from the antenna at specific frequency. Largest relative differences are captured at 10 GHz:  $sPD_{tot}$  averaged on the spherical averaging surface is 2.92% lower than the one averaged on the “near” planar surface at  $d = 10$  mm, while at  $d = 2$  mm,  $sPD_{tot}$  averaged on the spherical averaging surface is 18.54% and 31.31% larger compared to the one averaged on the “mid” and “far” planar surfaces, respectively. Above 30 GHz, relative differences between  $sPD_{tot}$  on the spherical and “near” planar averaging surfaces are within 1% regardless of  $d$ . For a full visual comparison of relative differences between  $sPD_{tot}$  averaged over a spherical and planar surfaces, see Fig. 7.

### C. Normal Component Definition Versus the Norm Definition on Spherical Model

Even though the functional dependence on the separation distance between the antenna and averaging surfaces is similar,  $sPD_{tot}$  results in higher values and could offer a more conservative estimate compared to  $sPD_n$ . This is most pronounced in near field conditions, explored in detail in [33] at similar frequencies and separation distances as in this study, but extended with a variety of antenna types. Li *et al.* [33] stated that the choice of the definition of the spatially averaged IPD yields in marginal calculation errors of exposure assessment, however, without taking into account the effect of curvature of an averaging surface.

Here, we compare two definitions of the spatially averaged IPD by considering a spherical averaging surface and exposure at the transition frequency for BR/DRL (6 GHz), and at the

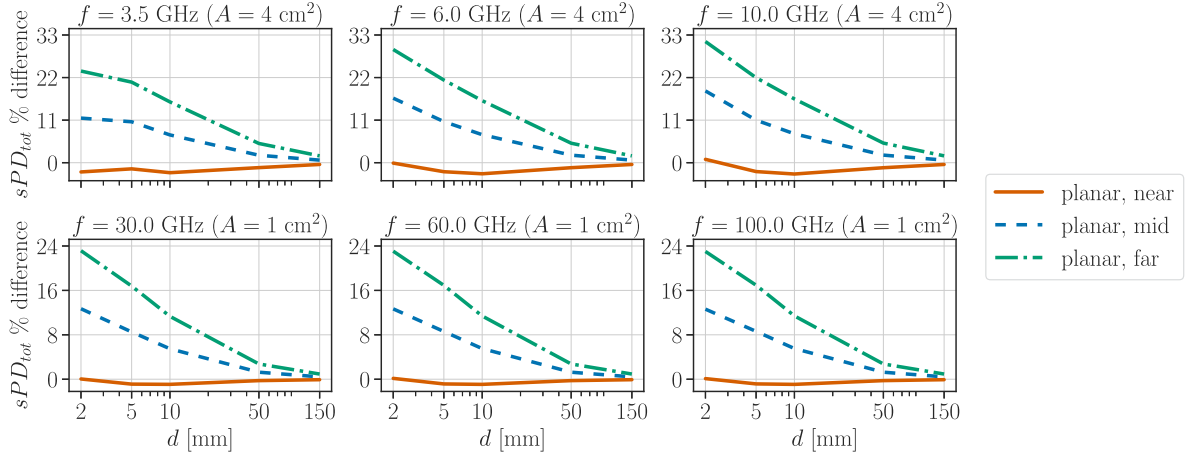


Fig. 7. Relative differences between  $sPD_{tot}$  averaged over 3 planar surfaces (“near,” “mid” and “far”) and a spherical surface as functions of the separation distance from the antenna at 3.5 GHz, 6 GHz, and 10 GHz (first row), and at 30 GHz, 60 GHz, and 100 GHz (second row).

TABLE I  
ABSOLUTE PERCENTAGE DIFFERENCES BETWEEN  $sPD_n$  AND  $sPD_{tot}$  ON A SPHERICAL SURFACE AT DIFFERENT SEPARATION DISTANCES FROM THE ANTENNA AT 6 AND 30 GHz

	$d$ [mm]	2	5	10	50	150
6 GHz	$sPD_n$ [W/m <sup>2</sup> ]	8.3	5.54	3.03	0.22	0.03
	$sPD_{tot}$ [W/m <sup>2</sup> ]	12.16	6.69	3.27	0.22	0.03
	% difference*	37.79	18.94	7.75	0.16	0.07
30 GHz	$sPD_n$ [W/m <sup>2</sup> ]	27.18	12.93	4.81	0.23	0.03
	$sPD_{tot}$ [W/m <sup>2</sup> ]	36.04	14.44	5.01	0.23	0.03
	% difference*	28.04	11.07	4.02	0.06	0.02

\*The reference is the average of compared values.

frequency of the averaging area reduction from 4 cm<sup>2</sup> to 1 cm<sup>2</sup> (30 GHz). Summarized results are available in Table I. Above 6 GHz, EM fields generally have the same electrical properties of a plane wave and far field exposure conditions are assumed. The reactive near field exists only in the immediate vicinity of an antenna, where the typical margin between the reactive and the radiative near field is defined as  $d_m = \lambda / (2\pi)$  [6]. This margin is  $\sim 8$  mm and  $\sim 1.69$  mm at 6 GHz and 30 GHz, respectively. Free space assessment should be sufficiently accurate to ensure safety limits compliance at 30 GHz [34], however, at lower frequencies relevant near field exposure should not be neglected [35]. The relative difference between  $sPD_n$  and  $sPD_{tot}$  in the reactive near field at 6 GHz and 30 GHz is the largest and it amounts to 37.79% and 28.04%, respectively, where  $sPD_{tot}$  could potentially be a more conservative exposure estimate, which should be additionally verified with thermal dosimetry analysis. For  $d > 2$  mm, i.e., after reactive near field conditions are no longer present, relative differences between  $sPD_n$  and  $sPD_{tot}$  at 30 GHz are marginal. The same goes for  $d \geq 10$  mm at 6 GHz, where relative differences are within 8%.

Overall, relative differences in the reactive near field are significant and one should be very cautious when considering the choice of the RL/ERL. It is stated in [6] that the use of the IPD in reactive near field conditions does not appropriately

correlate with the APD and that BR/DRL should be used instead. However, recent numerical results from [25] demonstrate  $sPD_{tot}$  to correlate slightly better with skin temperature in comparison to  $sPD_n$ , but only simplistic evaluation planes have been considered.

#### IV. CONCLUSION

We propose a technique for the accurate assessment of the spatially averaged IPD over a spherical model of a human head to account for more realistic exposure scenarios by considering a nonplanar averaging surface. To validate this approach, two definitions of the spatially averaged IPD have been considered: 1) the normal component of the IPD across an averaging surface ( $sPD_n$ ), and 2) the norm, i.e., the magnitude, of the IPD ( $sPD_{tot}$ ). The IPD averaged spatially over three planar surfaces placed in different locations with respect to a spherical surface fixed in space, and a spherical averaging surface itself are assessed. Comparative analysis is performed for the EM exposure where the source is defined as a half-wavelength dipole antenna operating between 3.5 GHz and 100 GHz.

According to the studied exposure scenarios, results indicate that some discrepancies between the IPD averaged on a spherical and planar surfaces occur. In the worst case scenario, relative differences reach up to 28.35% and 31.31% for  $sPD_n$  and  $sPD_{tot}$ , respectively, at certain conditions ( $f = 10$  GHz,  $d = 2$  mm) when the “far” planar averaging surface is considered. However, the relative difference is less significant if more appropriate settings are observed, i.e., averaging performed on the “near” planar surface—the surface that lies on a tangent plane to a spherical averaging surface in the nearest point relative to the antenna. The largest relative difference between  $sPD_n$  on a spherical and the “near” planar surface is 11.11% at 10 GHz and  $d = 2$  mm. On the other hand, the largest relative difference between  $sPD_{tot}$  on a spherical and the “near” planar surface is  $-2.92\%$  at 10 GHz and  $d = 10$  mm. Irrespective of the definition, all relative differences (apart between  $sPD_{tot}$  on a spherical and the “near” planar surface) are expressed as positive percentages that decrease with an increase in  $d$  and become negligible

(within 2%) at  $d \geq 50$  mm. Above 30 GHz, the reduction in the averaging surface area is applied after which the spatially averaged IPD stays relatively unchanged. Overall, regardless of both frequency and separation distance, averaging over a spherical surface results in larger values of  $sPD_n$  while similar values of  $sPD_{tot}$  compared to averaging on the “near” planar surface.

Furthermore, a comparative analysis between  $sPD_n$  and  $sPD_{tot}$  averaged on a spherical model is performed at characteristic frequencies of 6 GHz and 30 GHz. The maximal relative difference is observed in the reactive near field at 6 GHz, where  $sPD_{tot}$  is 37.79% larger than  $sPD_n$ , with the reference being the average of compared values. Relative differences become marginal after reactive near field conditions are no longer present.

The effect of the curvature of the spherical averaging surface above 6 GHz and its implication on the overall spatially averaged IPD from the presented results could potentially be useful for consideration in the future version of guidelines and standards.

#### APPENDIX A DIPOLE ANTENNA MODELING

The current distribution over a center-fed half-wavelength dipole antenna of radius  $a$  and length  $L$  is governed by the Pocklington integro-differential equation [30]

$$E_x^{exc} = j\omega \frac{\mu_0}{4\pi} \int_{-L/2}^{L/2} I(x') g_a(x, x') dx' - \frac{1}{j4\pi\omega\epsilon_0} \frac{\partial}{\partial x} \int_{-L/2}^{L/2} \frac{\partial I(x')}{\partial x'} g_a(x, x') dx' \quad (A.1)$$

where  $I(x')$  is the current distribution,  $g_a(x, x')$  is the integral equation kernel of free space

$$g_a(x, x') = \frac{\exp(-jkR_a)}{R_a} \quad (A.2)$$

and  $R_a$  represents the Euclidian distance from the source point at the center of the wire,  $x'$ , to the observation point on the outer layer of the wire,  $x$ . For a schematic visual representation of a dipole in free space, see Fig. 8. Other parameters in (A.1) are in order: angular frequency,  $\omega$ , permeability of free space,  $\mu_0$ , and permittivity of free space,  $\epsilon_0$ , with  $k$  being the wave number in (A.2). The spatial discretization of the dipole is performed by using 51 wire segments with the radius of the wire being set to 1/10 of a single segment's length. The solution of (A.1) is carried out by the Galerkin–Bubnov indirect boundary element method [30].

Provided the current distribution is known, electric field components can be obtained at each point on the surface of a model by following integral expressions [30]:

$$E_x = \frac{1}{j4\pi\omega\epsilon_0} \left( \int_{-L/2}^{L/2} \frac{\partial I(x')}{\partial x'} \frac{\partial g(x, y, z, x')}{\partial x} dx' - k^2 \int_{-L/2}^{L/2} I(x') g(x, y, z, x') dx' \right) \quad (A.3)$$

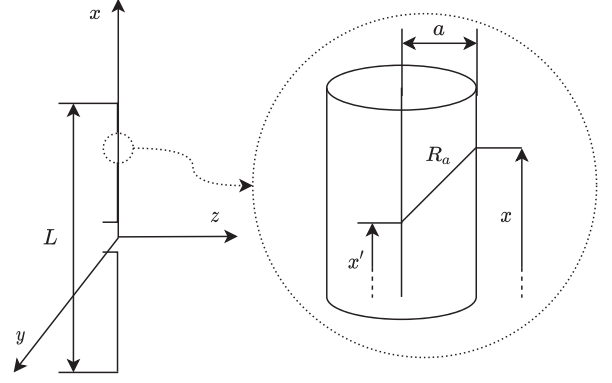


Fig. 8. Center-fed half-wavelength dipole in free space.

$$E_y = \frac{1}{j4\pi\omega\epsilon_0} \int_{-L/2}^{L/2} \frac{\partial I(x')}{\partial x'} \frac{\partial g(x, y, z, x')}{\partial y} dx' \quad (A.4)$$

$$E_z = \frac{1}{j4\pi\omega\epsilon_0} \int_{-L/2}^{L/2} \frac{\partial I(x')}{\partial x'} \frac{\partial g(x, y, z, x')}{\partial z} dx' \quad (A.5)$$

where  $g(x, y, z, x')$  is the Green function in free space

$$g(x, y, z, x') = \frac{\exp(-jkR)}{R} \quad (A.6)$$

and  $R$  represents the Euclidian distance from the source point,  $x'$ , to the observation point on the surface of a model,  $(x, y, z)$ . Magnetic field components, derived from the Maxwell–Faraday law [30], are given by

$$H_y = \frac{1}{4\pi} \int_{-L/2}^{L/2} I(x') \frac{\partial g(x, y, z, x')}{\partial z} dx' \quad (A.7)$$

$$H_z = -\frac{1}{4\pi} \int_{-L/2}^{L/2} I(x') \frac{\partial g(x, y, z, x')}{\partial y} dx' \quad (A.8)$$

Equations (A.3)–(A.5), (A.7), and (A.8) are computed numerically by using boundary element formalism and enforcing automatic differentiation, which has been shown to be far superior by means of speed and accuracy compared to numerical differentiation [36].

#### REFERENCES

- [1] J. G. Andrews *et al.*, “What will 5G be?,” *IEEE J. Sel. Areas Commun.*, vol. 32, no. 6, pp. 1065–1082, Jun. 2014.
- [2] T. S. Rappaport *et al.*, “Millimeter wave mobile communications for 5G cellular: It will work!,” *IEEE Access*, vol. 1, pp. 335–349, 2013.
- [3] M. Zhadobov, N. Chahat, R. Sauleau, C. Le Quement, and Y. Le Drian, “Millimeter-wave interactions with the human body: State of knowledge and recent advances,” *Int. J. Microw. Wireless Technol.*, vol. 3, no. 2, pp. 237–247, 2011.
- [4] T. Wu, T. S. Rappaport, and C. M. Collins, “Safe for generations to come: Considerations of safety for millimeter waves in wireless communications,” *IEEE Microw. Mag.*, vol. 16, no. 2, pp. 65–84, 2015.
- [5] K. R. Foster, M. C. Ziskin, Q. Balzano, and A. Hirata, “Thermal analysis of averaging times in radio-frequency exposure limits above 1 GHz,” *IEEE Access*, vol. 6, pp. 74536–74546, 2018.
- [6] International commission on non-ionizing radiation protection (ICNIRP), “guidelines for limiting exposure to electromagnetic fields (100 kHz to 300 GHz),” *Health Phys.*, vol. 118, pp. 483–524, 2020.
- [7] “IEEE Standard for safety levels with respect to human exposure to electric, magnetic, and electromagnetic fields, 0 Hz to 300 GHz,” IEEE

- Std C95.1–2019 (Revision of IEEE Std C95.1–2005/ Incorporates IEEE Std C95.1–2019/Cor 1–2019), pp. 1–312, 2019.
- [8] Y. Hashimoto *et al.*, “On the averaging area for incident power density for human exposure limits at frequencies over 6 GHz,” *Phys. Med. Biol.*, vol. 62, no. 8, pp. 3124–3138, 2017.
  - [9] K. R. Foster, M. C. Ziskin, and Q. Balzano, “Thermal response of human skin to microwave energy: A critical review,” *Health Phys.*, vol. 111, no. 6, pp. 528–541, 2016.
  - [10] K. Li, K. Sasaki, K. Wake, T. Onishi, and S. Watanabe, “Quantitative comparison of power densities related to electromagnetic near-field exposures with safety guidelines from 6 to 100 GHz,” *IEEE Access*, vol. 9, pp. 115801–115812, 2021.
  - [11] A. Hirata, “Review on human dosimetry for radio-frequency exposure above 6 GHz - international exposure standards,” in *Proc. Asia-Pacific Microw. Conf.*, 2018, pp. 681–683.
  - [12] A. Hirata, D. Funahashi, and S. Kodera, “Setting exposure guidelines and product safety standards for radio-frequency exposure at frequencies above 6 GHz: Brief review,” *Ann. Telecommun.*, vol. 74, pp. 17–24, 2019.
  - [13] A. Hirata *et al.*, “Human exposure to radiofrequency energy above 6 GHz: Review of computational dosimetry studies,” *Phys. Med. Biol.*, vol. 66, no. 8, 2021, Art. no. 08TR01.
  - [14] K. R. Foster, M. C. Ziskin, and Q. Balzano, “Thermal modeling for the next generation of radiofrequency exposure limits: Commentary,” *Health Phys.*, vol. 113, no. 1, pp. 41–53, 2017.
  - [15] M. C. Ziskin, S. I. Alekseev, K. R. Foster, and Q. Balzano, “Tissue models for RF exposure evaluation at frequencies above 6 GHz,” *Bioelectromagnetics*, vol. 39, no. 3, pp. 173–189, 2018.
  - [16] K. R. Foster, M. C. Ziskin, Q. Balzano, and G. Bit-Babik, “Modeling tissue heating from exposure to radiofrequency energy and relevance of tissue heating to exposure limits: Heating factor,” *Health Phys.*, vol. 115, no. 2, pp. 295–307, 2018.
  - [17] D. Funahashi, T. Ito, A. Hirata, T. Iyama, and T. Onishi, “Averaging area of incident power density for human exposure from patch antenna arrays,” *IEICE Trans. Electron.*, vol. E101.C, no. 8, pp. 644–646, 2018.
  - [18] T. Nakae, D. Funahashi, J. Higashiyama, T. Onishi, and A. Hirata, “Skin temperature elevation for incident power densities from dipole arrays at 28 GHz,” *IEEE Access*, vol. 8, pp. 26863–26871, 2020.
  - [19] W. He, B. Xu, M. Gustafsson, Z. Ying, and S. He, “RF compliance study of temperature elevation in human head model around 28 GHz for 5G user equipment application: Simulation analysis,” *IEEE Access*, vol. 6, pp. 830–838, 2018.
  - [20] D. Poljak and M. Cvetković, “On the incident power density calculation in GHz frequency range: A case of hertz dipole,” in *Proc. 4th Int. Conf. Smart Sustain. Technol.*, 2019, pp. 1–4.
  - [21] W. He, Z. Ying, and S. He, “EMF exposure analysis of combining specific absorption rate and incident power density using canonical dipoles,” in *Proc. 13th Eur. Conf. Antennas Propag.*, 2019, pp. 1–5.
  - [22] W. He, B. Xu, Y. Yao, D. Colombi, Z. Ying, and S. He, “Implications of incident power density limits on power and EIRP levels of 5G millimeter-wave user equipment,” *IEEE Access*, vol. 8, pp. 148214–148225, 2020.
  - [23] A. Christ, T. Samaras, E. Neufeld, and N. Kuster, “Limitations of incident power density as a proxy for induced electromagnetic fields,” *Bioelectromagnetics*, vol. 41, pp. 348–359, 2020.
  - [24] Y. Diao *et al.*, “Effect of incidence angle on the spatial-average of incident power density definition to correlate skin temperature rise for millimeter wave exposures,” *IEEE Trans. Electromagn. Compat.*, vol. 63, no. 5, pp. 1709–1716, Oct. 2021.
  - [25] “IEEE guide for the definition of incident power density to correlate surface temperature elevation,” IEEE Std 2889–2021, pp. 1–152, 2021.
  - [26] T. Walters, D. Blick, L. Johnson, E. Adair, and K. Foster, “Heating and pain sensation produced in human skin by millimeter waves: Comparison to a simple thermal model,” *Health Phys.*, vol. 78, no. 3, pp. 259–267, 2000.
  - [27] M. Kojima *et al.*, “Ocular effects of exposure to 40, 75, and 95 GHz millimeter waves,” *J. Infrared Millimeter, Terahertz Waves*, vol. 39, no. 9, pp. 1866–1896, 2018.
  - [28] Y. Diao, E. A. R. Rashed, and A. Hirata, “Assessment of absorbed power density and temperature rise for nonplanar body model under electromagnetic exposure above 6 GHz,” *Phys. Med. Biol.*, vol. 65, no. 22, 2020, Art. no. 224001.
  - [29] D. Poljak *et al.*, “On the use of conformal models and methods in dosimetry for nonuniform field exposure,” *IEEE Trans. Electromagn. Compat.*, vol. 60, no. 2, pp. 328–337, 2018.
  - [30] D. Poljak, *Advanced Modeling in Computational Electromagnetic Compatibility*. Hoboken, NJ, USA: Wiley, 2006.
  - [31] Z. Zhuang, D. Landsittel, S. Benson, R. Roberge, and R. Shaffer, “Facial anthropometric differences among gender, ethnicity, and age groups,” *Ann. Occup. Hyg.*, vol. 54, no. 4, pp. 391–402, 2010.
  - [32] M. Abramowitz and I. A. Stegun, *Handbook of Mathematical Functions With Formulas, Graphs, and Mathematical Tables*. Mineola, NY, USA: Dover Publication, 1972, ch. 25.4.29.
  - [33] K. Li *et al.*, “Intercomparison of calculated incident power density and temperature rise for exposure from different antennas at 10–90 GHz,” *IEEE Access*, vol. 9, pp. 151654–151666, 2021.
  - [34] D. Colombi, B. Thors, C. Törnevik, and Q. Balzano, “RF energy absorption by biological tissues in close proximity to millimeter-wave 5G wireless equipment,” *IEEE Access*, vol. 6, pp. 4974–4981, 2018.
  - [35] E. Carrasco, D. Colombi, K. R. Foster, M. Ziskin, and Q. Balzano, “Exposure assessment of portable wireless devices above 6 GHz,” *Radiat. Protection Dosimetry*, vol. 183, no. 4, pp. 489–496, 2018.
  - [36] A. Lojić Kapetanović and D. Poljak, “Application of automatic differentiation in electromagnetic dosimetry: Assessment of the absorbed power density in the mmWave frequency spectrum,” in *Proc. 6th Int. Conf. Smart Sustain. Technol. (SpliTech)*, pp. 1–6, 2021.



**Ante Lojić Kapetanović** (Graduate Student Member, IEEE) was born in Split, Croatia, in 1995. He received the B.S. and M.S. degrees in electrical engineering with the Faculty of Electrical Engineering, Mechanical Engineering, and Naval Architecture (FESB), University of Split, Croatia, in 2017 and 2019, respectively. Since 2020, he has been working toward the Ph.D. degree in computational bioelectromagnetics with the University of Split.

He did a three-month research visit with the Aalborg University, Aalborg, Denmark, during his M.S., and a one-month research visit with the IETR/CNRS, France in 2021. He has authored or coauthored two journal and more than 10 conference papers in different areas of computational sciences. His research interests include computational dosimetry, electromagnetic compatibility of a biological neuron and neural networks, modeling the biological dynamical systems and system identification, and scientific machine learning-emerging methods such as physics-informed neural networks. The focus of the research, however, is human exposure to electromagnetic fields, especially at millimeter waves.

Mr. Lojić Kapetanović has been a member of the Croatian Chapter of the IEEE EMC Society, since 2020, and from 2021, he has been a Student Member of the European BioElectromagnetics Association (EBEA). He was the recipient of the Best Student Paper Award at the 2022 IEEE MTT-S International Microwave Biomedical Conference in Sozhou, China.



**Dragan Poljak** (Senior Member, IEEE) received the Ph.D. degree in electrical engineering from the University of Split, Split, Croatia, in 1996.

He is a Full Professor with the Department of Electronics and Computing, University of Split. He has authored or coauthored more than 160 journals and 250 conference papers, and authored some books, e.g., two by Wiley, *Computational Methods in Electromagnetic Compatibility: Antenna Theory Approach versus Transmission Line Models* (Wiley, 2018), *Advanced Modeling in Computational Electromagnetic*

*Compatibility* (Wiley, 2007), and one by Elsevier, *Human Interaction with Electromagnetic Fields: Computational Models in Dosimetry* (Academic, 2019). He is currently involved with the ITER Physics EUROfusion Collaboration and with the Croatian Center for Excellence in Research for Technical Sciences. His research interests include computational electromagnetics, electromagnetic compatibility, bioelectromagnetics, and plasma physics.

Dr. Poljak is a Member of the Editorial Board of Engineering Analysis with Boundary Elements, Mathematical Problems in Engineering, and IET Science, Measurement, and Technology. From 2013 to 2021, he was a Member of the Board of the Croatian Science Foundation. He is active in several working groups of the IEEE/International Committee on Electromagnetic Safety (ICES) Technical Committee 95, and SC6 EMF Dosimetry Modeling. He was the recipient of several prizes for his achievements, such as the National Prize for Science (2004), Croatian Section of the IEEE Annual Award (2016), Technical Achievement Award of the IEEE EMC Society (2019), and George Green Medal from the University of Mississippi (2021).